



Photogeneration of reactive oxygen species from biochar suspension for diethyl phthalate degradation



Guodong Fang^a, Cun Liu^a, Yujun Wang^a, Dionysios D. Dionysiou^b, Dongmei Zhou^{a,*}

^a Key Laboratory of Soil Environment and Pollution Remediation, Institute of Soil Science, Chinese Academy of Sciences, Nanjing 210008, P.R. China

^b Environmental Engineering and Science Program, University of Cincinnati, Cincinnati, OH 45221-0012, USA

ARTICLE INFO

Article history:

Received 22 March 2017

Received in revised form 4 May 2017

Accepted 10 May 2017

Available online 11 May 2017

Keywords:

Biochar

Photochemical reactions

ROS

DEP degradation

PFRs

ABSTRACT

In this study, the photogeneration of reactive oxygen species (ROS) from biochar suspension was investigated. The characterizations of biochar particles before and after photochemical reactions were analyzed by using FTIR, Raman, XPS and electron paramagnetic resonance (EPR) techniques. It was found that the model pollutant diethyl phthalate (DEP) was efficiently degraded and partially mineralized under UV and simulated solar lights in biochar suspension, with hydroxyl radicals ($\cdot\text{OH}$) and singlet oxygen ($^1\text{O}_2$) as the dominant ROS. EPR coupled with chemical probe methods and free radical quenching studies were used to quantify and elucidate the formation mechanism of $\cdot\text{OH}$ and $^1\text{O}_2$. The results indicated that biochar carbon matrix (BCM) accounted for 63.6%–74.6% of $\cdot\text{OH}$ and 10%–44.7% of $^1\text{O}_2$ formation, while dissolved organic matter (DOM) derived from biochar generated 46.7%–86.3% of $^1\text{O}_2$ and 3.7%–12.5% of $\cdot\text{OH}$. BCM-bound persistent free radicals (BCM-PFRs) and quinone-like structure of BCM (BCM-Q) were the predominant factors affecting $\cdot\text{OH}$ and $^1\text{O}_2$ formation from BCM under light. Detailed ROS generation pathways are proposed as: (i) DOM from biochar particles contributes to $\cdot\text{OH}$ and $^1\text{O}_2$ formation via light-induced energy and electron transfer processes; (ii) BCM-Q forms excited triplet states ($^3[\text{BCM-Q}]^*$) under light irradiation and induces the formation $^1\text{O}_2$; (iii) UV promotes the formation of BCM-PFRs, which transfer electrons to oxygen to form superoxide anion radical (O_2^-), further yielding H_2O_2 ; and (iv) H_2O_2 -dependent pathways including BCM-PFRs activation and photo-Fenton reaction are primarily responsible for $\cdot\text{OH}$ production. Furthermore, BCM exhibits the excellent reusability towards DEP degradation during the three cycles under light.

© 2017 Elsevier B.V. All rights reserved.

1. Introduction

Heterogeneous photocatalysis based on semiconductors is becoming one of the most promising technologies in the environmental remediation since the pioneering studies in 1977 reporting the ability of titania powders to decompose cyanides under light in aqueous solutions [1]. Besides titania, extensive research has been carried out to develop more efficient photocatalysts such as ZnO, ZrO_2 , CeO_2 , and sulfides (CdS , ZnS) etc. aiming at fast and complete degradation of various contaminants [2–7]. However, most of these photocatalysts need expensive/scarce metal species that limits their long term and large scale applications. Therefore, it is imperative to develop easily-accessible, metal-free and environmentally friendly photocatalysts for the degradation of contaminants.

Carbon is a strong light absorbing material, and the use of carbon materials, e.g., activated carbon (AC), as supports or modifiers of conventional semiconductor photocatalysts in heterogeneous photocatalysis has attracted much research efforts in recent years [8–10]. AC exhibits a reasonably high efficiency to enhance the photocatalytic ability of TiO_2 [11–13]. Furthermore, under light irradiation, ACs were observed to induce the formation of reactive oxygen species (ROS) such as $\cdot\text{OH}$, singlet oxygen ($^1\text{O}_2$), superoxide radical anion (O_2^-), and hydrogen peroxide (H_2O_2), in the absence of conventional semiconductors, although the mechanism was unclear [14–16]. A recent study by Velo-Gala et al. found that the surface chemistry of AC plays an important role in its photocatalytic activity under UV or solar light [17]. The photochemical properties of new carbon materials, such as fullerenes (C_{60}), graphene oxide and carbon nanotubes, are also of great interest to environmental scientists due to their photocatalytic performance [18–21]. Although the ability of carbon materials to produce ROS under light has received considerable attention, most previous studies focused on their light induced toxicity effects [22,23]. Meanwhile, little

* Corresponding author.

E-mail address: dmzhou@issas.ac.cn (D. Zhou).

attention has been paid to the feasibility of carbon-produced ROS on the transformation of contaminants.

Biochar is an emerging carbon material, mainly produced by biomass pyrolysis, and has received increasing attention due to its extensive uses and benefits as fertilizer, carbon sequestration and soil amendment in agricultural and environmental fields in recent years [24–28]. The practical land application of biochar has led to an increase in biochar particles released into aquatic systems. Wang et al. found that small size biochar particles have a high probability of leaching into groundwater and facilitating the transport of adsorbed contaminants [29]. More importantly, the dissolvable fractions of biochar contribute substantially to the dissolved organic matter (DOM), and thus are readily released into surface water, especially in riparian areas [30,31]. Jaffe et al. found that dissolved black carbon accounts for about 10% of global riverine flux of dissolved organic carbon [32]. Consequently, exploration of the photochemical properties of biochar particles and the related ROS formation mechanism from biochar are crucial to assess its environmental impact, because in general, ROS plays an important role in contaminant transformations by photochemical processes in natural aquatic systems [33–37]. Furthermore, examination of photochemical behavior of biochar could be beneficial for developing new hybrid materials with the conventional metal photocatalysts for the sustainable water remediation and treatment.

Our group and others found the catalytic properties of biochar play an important role in contaminant transformations in aquatic systems [38–40]. Persistent free radicals (PFRs) in biochar can catalyze H_2O_2 and persulfate decomposition in aqueous phase to form free radicals [38–40]. PFRs in biochar and other carbon materials also mediate hydroxyl radical ($\cdot\text{OH}$) formation and degrade contaminants in the presence of dioxygen without additional oxidants [41–44]. Furthermore, biochar can act as an electron shuttle to mediate Fe_2O_3 reduction and promote microbial NH_4^+ oxidation and NO_3^- reduction [45–47]. Recently, the dissolvable portion of biochar was found to exhibit photocatalytic ability and induce the ROS formation under light [48]. By using chemical probe methods, the light-induced ROS formation pathway on dissolved biochar was deduced to be similar to the pathway for natural DOM [33–37,48]. However, the roles of biochar particles (e.g., carbon matrix) in ROS formation, the extent of ROS contribution to contaminant degradation, and the underlying mechanism of ROS formation under light are not fully understood.

We therefore hypothesized that biochar particles exhibit similar photochemical properties to other carbon materials. The main objectives of this study were to investigate the photocatalytic formation of ROS in biochar suspension under light for contaminant degradation, and elucidate the related reaction mechanisms. The characterizations of biochar particles before and after photochemical reactions were analyzed by FTIR, Raman, X-ray photoelectron spectroscopies (XPS) and electron paramagnetic resonance (EPR) techniques. The formation and steady-state concentrations of ROS, such as $\cdot\text{OH}$ and $\cdot\text{O}_2$, were determined using EPR and chemical probe methods, respectively. Diethyl phthalate (DEP) was selected as the target pollutant because it is a USEPA priority environmental pollutant and its degradation mechanism by $\cdot\text{OH}$ is well established [49].

2. Materials and methods

2.1. Materials

Chemicals used in this study are described in the Supporting Information (SI; Text S1) and the preparation of biochar is described in Text S2 in the SI, following the similar procedure as described in detail in our previous studies [40,41]. Briefly, four different biochars

were made and named as P300, P500, W300, and W500, respectively, according to the source materials (P as pine needles and W as wheat straws) and pyrolysis temperatures (300 and 500 °C). The characterizations of biochar were examined by using techniques including elemental analysis, EPR, and FTIR, Raman, and XPS.

2.2. Photochemical experiments

Prior to the light irradiation, the biochar suspensions (200 mg L⁻¹) in borosilicate glass tubes (100 mL) sealed with PTFE screw caps were dispersed by ultrasonication for 30 min, and then DEP stock solution was spiked in to obtain a concentration of 20 mg L⁻¹. The mixture was agitated for 2 h in dark to reach apparent adsorption equilibrium. The aqueous DEP concentrations at equilibrium decreased to 19.2 mg L⁻¹, 18.8 mg L⁻¹, 19.3 mg L⁻¹, and 18.4 mg L⁻¹ in P300, P500, W300, and W500 suspensions, respectively, which indicated that adsorption contributed to 4–8% of DEP removal from solution within 2 h. All light irradiation experiments were conducted after 2 h adsorption, and phosphate buffer solution (PBS; 10 mM) was added in the biochar suspensions (200 mg L⁻¹) to fix pH at 7.0 to minimize the effects of pH on the photochemical processes. The borosilicate glass tubes were placed in a photochemical reactor (XPA-7, Nanjing Xujiang Electromechanical Plant, China) and rotated at 500 rpm to ensure uniform light exposure and a well-mixed biochar suspension. A 100-W low pressure mercury lamp (wavelength ranged from 350 to 450 nm and centered at 365 nm) was placed in a quartz cooling pipe positioned vertically in the center of the photochemical reactor. The reaction temperature was controlled at 25 °C and the light intensity at 365 nm in the borosilicate glass tube was 2.3×10^{-5} Einstein cm⁻² s⁻¹. The schematic diagram of the photochemical reactor was depicted in our previous study [50]. Control experiments without addition of biochar particles were conducted under the same reaction conditions. Dark control experiments were also performed by wrapping the glass tubes with aluminum foil. In addition to UV light, a 500-W xenon lamp was used to simulate solar light, and ROS formation was determined under the simulated solar light at the same reaction conditions. The emission spectra of the xenon lamp are shown in Fig. S1 (provided by Nanjing Xujiang Electromechanical Plant, China).

DOM was extracted from the biochar suspensions to assess the contribution of the dissolved portion of biochar to ROS formation, as follows: biochar particles (0.5 g) were dispersed by ultrasonication in borosilicate glass tubes containing DI water (50 mL), and then agitated on a photochemical reactor at 500 rpm at room temperature (25 °C) without UV light for 2 h. Then, the suspension was passed through a 0.45-μm membrane filter and the photochemical experiments in the filtrate were conducted under UV light. The DOM concentration was determined by a total organic carbon (TOC) analyzer (Multi N/C 3000, Analytik Jena AG, Germany). The fluorescence excitation–emission matrix (EEMs) spectrum of DOM was obtained with a F-7000 fluorescence spectrophotometer (F-7000; Hitachi, Japan).

To examine the contribution of the solid biochar carbon matrix to ROS formation, photochemical experiments were conducted with HCl–HF treated biochar particles under the same conditions as those for untreated biochar. HCl–HF treated biochar particles were prepared by following procedure to fully remove DOM but retain PFRs in biochar particles. Biochar (10 g) was first washed with 1 M HCl solution (500 mL) and then HCl–HF solution (500 mL, 1.0 M, 1:1 v/v) several times until the DOM concentration was below the detection limit (<0.1 mg L⁻¹). The biochar sample was then washed twice with DI water to remove soluble salts, and freeze-dried prior to use. The process for the determination of reactive oxygen species was presented in the SI (Text S3 and S4). All the experiments were

performed in triplicate and results were reported as the mean with standard deviations.

3. Results and discussion

3.1. Characterization of biochar particles

Table S1 shows the elemental composition of biochar particles used in this study. The results showed that biochar pyrolyzed at higher temperatures had a greater carbon content than biochar pyrolyzed at lower temperatures. The N and Fe contents were about 1.1%–1.2% and 1.1–1.8 mg/kg for all biochars, respectively. The structures and morphologies of the biochar particles were characterized by FTIR, Raman, XPS, and EPR techniques. The FTIR spectra showed that the peak intensities of some aliphatic functional groups, such as —OH ($3437\text{--}3453\text{ cm}^{-1}$), —CH_3 ($2963\text{--}2966\text{ cm}^{-1}$), aromatic C=O /quinone C=O (1613 cm^{-1}), and aromatic carbonyl/carboxyl/quinone C=O (1710 cm^{-1}) decreased with increasing biochar pyrolysis temperature, indicating a higher degree of carbonization in biochar produced at 500°C compared with biochar produced at 300°C (Fig. S2). XPS C 1s spectra were analyzed to reveal the carbon states in the biochar (Fig. S3). The biochar C 1s spectra were deconvoluted and fitted to several major components with chemical shifts corresponding to: C—C/Ar—C (aromatic carbon, $284.6\text{--}284.8\text{ eV}$), C defects ($285.1\text{--}285.2\text{ eV}$) and C—O ($286.8\text{--}287.2\text{ eV}$), among which C—C/Ar—C and C defects were predominant, accounting for 35.6%–52.2% and 35.2%–41.2%, respectively, of the total carbon contents on the biochar particle surfaces (Table S2).

Raman spectra results showed that all biochar samples had peaks at 1351 cm^{-1} (D band) and 1581 cm^{-1} (G band), suggesting the formation of graphitic carbon (Fig. S4). The G band represents the in-plane stretching motion of sp^2 carbon bonds, and the D band is usually related to disordered motions originating in symmetry broken structural defects or edges [51]. The peak intensity ratio of the D band and G band ($I_{\text{D}}/I_{\text{G}}$) has been suggested to be inversely proportional to the graphitization degree of carbon materials [51]. In this study, the $I_{\text{D}}/I_{\text{G}}$ ratios were 0.65, 0.70, 0.53, and 0.53 for P300, P500, W300, and W500, respectively, and followed the order P500 > P300 > W300 > W500, which indicated a much smaller size of the ordered graphite crystallite in pyrolyzed pine needle biochar (Table S3). EPR was used to further characterize the persistent free radicals in biochar, which were presumed to be related to its chemical or photochemical reactivities. As shown in Fig. S5 and Table S4, a singlet EPR signal with a line width of 4.5–6.5 G and g-factor of 2.0038–2.0045 representing the PFRs was observed for all biochar particles. The PFR concentrations were 19.6×10^{18} and 9.98×10^{18} spins/g for P500 and W500, respectively, which were significantly higher than those for P300 (4.57×10^{18} spins/g) and W300 (3.31×10^{18} spins/g). These results indicated that increasing the pyrolysis temperature favored PFR formation, in good agreement with previous studies [38].

3.2. DEP photodegradation with biochar particles under UV light

The kinetics of DEP (20 mg L^{-1}) degradation was examined in the presence of different biochar particles (0.2 g L^{-1}) under UV light at pH 7.0 (10 mM PBS). Fig. 1a showed that 58.9%, 72.3%, 52.3%, and 60.9% DEP degradations were achieved within 120 min by P300/UV, P500/UV, W300/UV, and W500/UV, respectively. In contrast, the DEP concentration only changed slightly under UV light in the absence of biochar, or in the biochar suspension without UV light (Fig. S6a). DEP degradation kinetics were fitted well with the pseudo-first-order equation (Fig. S6b), and the observed reaction rate constants (k_{obs}) were 0.0075 min^{-1} for P300/UV, 0.0108 min^{-1}

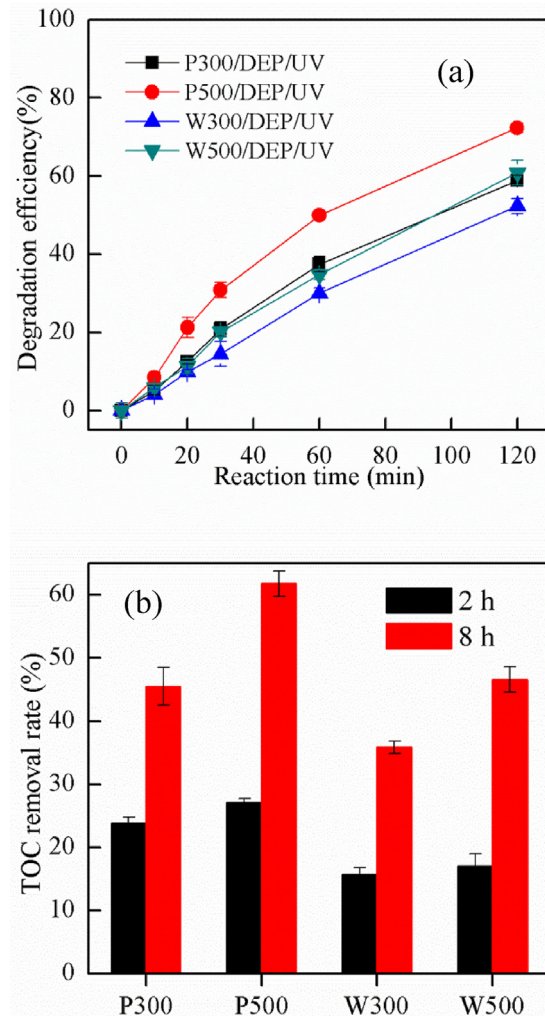


Fig. 1. Photodegradation of DEP under UV light in the presence of different biochar particles: (a) kinetics of DEP degradation, and (b) TOC removal rate of DEP calculated from the changes in the TOC of different reaction systems at 2 h and 8 h. Reaction conditions: $[\text{DEP}]_0 = 20\text{ mg L}^{-1}$, $[\text{biochar}]_0 = 0.2\text{ g L}^{-1}$, pH 7.0 (10 mM PBS), 100-W Hg lamp, and 25°C .

for P500/UV, 0.0063 min^{-1} for W300/UV, and 0.0079 min^{-1} for W500/UV, respectively. These results indicated that DEP was efficiently degraded in the biochar/UV system, and that the biochar samples exhibited different performance to induce DEP degradation in the following order: P500 > W500 \approx P300 > W300.

TOC removal rate is an important indicator for evaluating the photodegradation efficiency of organic contaminants, and therefore, was determined for the different biochar/UV systems. As shown in Fig. S7a, after the photoreactions, the TOC concentrations left in the supernatants were 16.6, 13.3, 21.2, and $16.5\text{ mg}_{\text{carbon}}\text{ L}^{-1}$ for P300/UV, P500/UV, W300/UV, and W500/UV, respectively, while it was $12.8\text{ mg}_{\text{carbon}}\text{ L}^{-1}$ for DEP/UV without biochar. The increase in the overall TOC concentrations could be related to the dissolution of biochar under UV irradiation. For biochar/UV in the absence of DEP, the TOC concentrations in the supernatants were 6.8, 4.0, 10.4, and $5.8\text{ mg}_{\text{carbon}}\text{ L}^{-1}$ for P300, P500, W300, and W500, respectively, which were markedly higher than the corresponding contents of 1.2, 1.1, 2.5, and $1.5\text{ mg}_{\text{carbon}}\text{ L}^{-1}$ for biochars without UV irradiation. The dissolution process was probably caused by the UV-induced decomposition of the surface functional groups of biochar, yielding low molecular compounds dissolved in the solution during the photocatalysis. The biochar dissolution contributions were deducted from the overall TOC concentrations

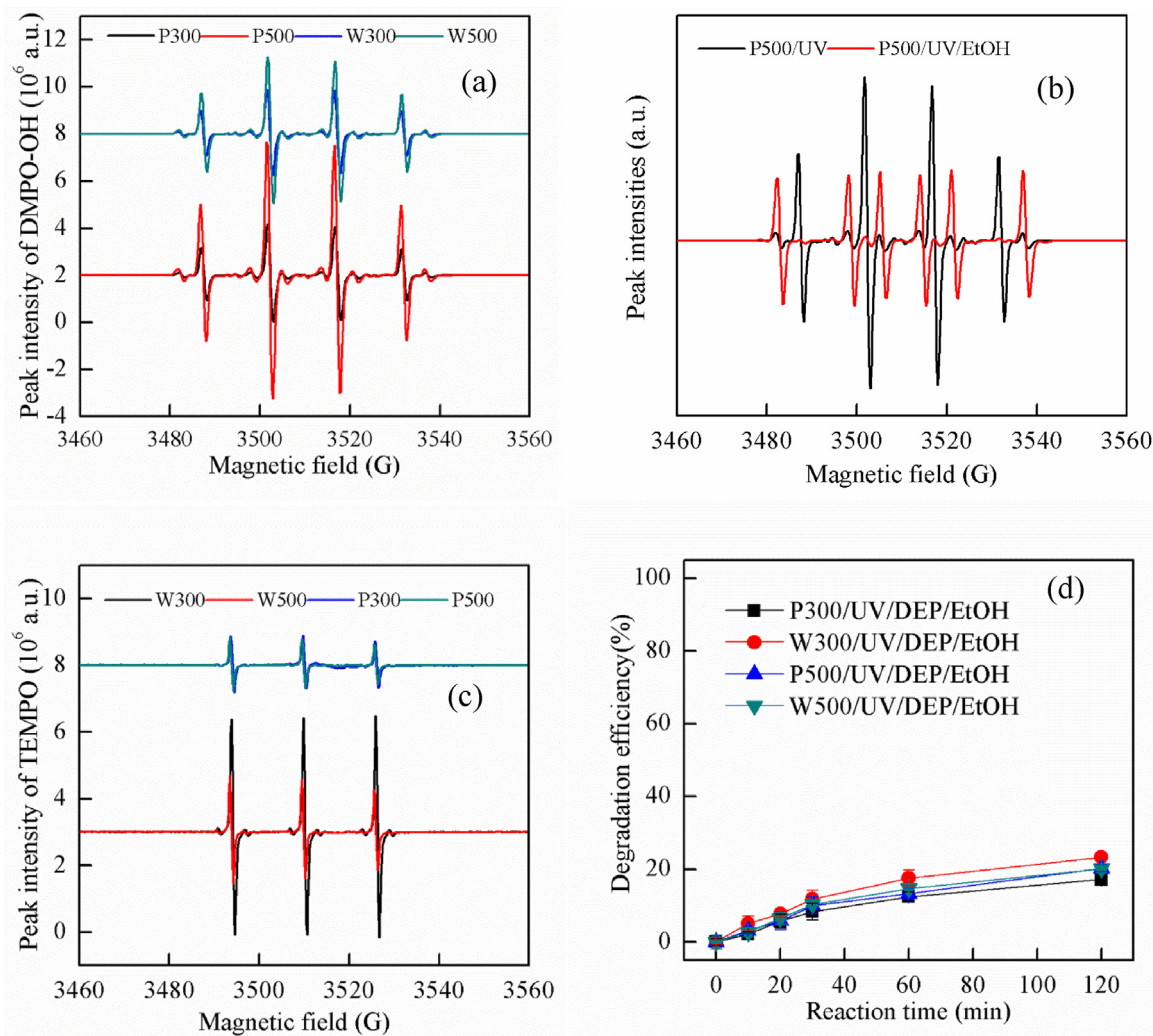


Fig. 2. EPR spectra of (a) DMPO—OH adducts in different biochar/UV systems irradiated for 2 min, and (b) EPR spectra of P500/UV suspension in the presence of ethanol (EtOH); (c) TEMPO spin adducts (from the reaction of TEMP and $^1\text{O}_2$) in biochar/UV irradiated for 2 min; (d) kinetics of DEP degradation in biochar/UV in the presence of EtOH. Reaction conditions: $[\text{biochar}]_0 = 0.2 \text{ g L}^{-1}$, $[\text{DMPO}]_0 = [\text{TEMP}]_0 = 100 \text{ mM}$, $[\text{DEP}]_0 = 20 \text{ mg L}^{-1}$, $[\text{EtOH}]_0 = 200 \text{ mM}$, $[\text{NaN}_3]_0 = 0.1 \text{ mM}$, pH 7.0 (10 mM PBS), 100-W Hg lamp, and 25 °C.

by subtracting the TOC concentrations in the biochar/UV blanks. The results showed that about 3.1, 3.5, 2.0, and 2.2 mg L⁻¹ TOC removals for DEP were achieved by P300/UV, P500/UV, W300/UV, and W500/UV, respectively, and corresponding TOC removal rate for DEP was 23.8%, 27.2%, 15.7% and 17.0% (Fig. 1b). The disappearance of DEP measured approached 100% with further prolonging the reaction time to 8 h (Fig. S7b), while TOC removal rate for DEP was increased to 45.5% for P300/UV, 61.8% for P500/UV, 35.8% for W300/UV and 46.6% for W500/UV, respectively. The discrepancy indicated partial mineralization of DEP was achieved in the biochar/UV systems.

3.3. Hydroxyl radical and singlet oxygen determination

Among the various ROS species produced from the photochemical reactions, •OH and $^1\text{O}_2$ usually exhibit the highest reactivities toward contaminant degradation [37]. Therefore, the formation and steady-state concentrations of •OH and $^1\text{O}_2$ generated in the biochar/UV system was determined in the present study.

3.3.1. EPR and free radical quenching studies

EPR coupled with spin-trapping agents 5,5-dimethyl-1-pyrrolidine N-oxide (DMPO) and 2,2,6,6-tetramethylpiperidine

(TEMP) was used to identify •OH and $^1\text{O}_2$, respectively. As illustrated in Fig. 2a, a significant four-line signal with an intensity ratio of 1:2:2:1 was observed in the biochar/UV systems in the presence of DMPO, which is the characteristic of DMPO—OH adducts. Moreover, the peak intensities of DMPO—OH varied markedly in different biochar suspensions, following the order: P500 > W500 > P300 > W300. Although the DMPO—OH signal was also observed in the blank DMPO solution under UV light, the weak signal was ascribed to direct irradiation of DMPO, not DMPO—OH adducts [52]. Ethanol (EtOH) quenching experiment was used to further confirm •OH formation in the biochar/UV suspension (Fig. 2b). The DMPO—OH signal was greatly suppressed in the presence of 200 mM EtOH, accompanied by the formation of DMPO—ethanol adducts (six lines with intensities of 1:1:1:1:1:1) in the P500/UV system as a result of the interaction between •OH and EtOH, which confirmed the formation of •OH in the biochar/UV systems.

Similarly, a three-line EPR signal with an intensity ratio of 1:1:1 was observed in the biochar/UV systems in the presence of TEMP, which is the characteristic of TEMPO adducts resulting from the oxidation of TEMP by $^1\text{O}_2$ (Fig. 2c). Furthermore, the TEMPO peak intensities varied in the different biochar samples in the following order: W300 > W500 > P300 > P500, which was coincident with the order of DOM concentrations released from biochars during the

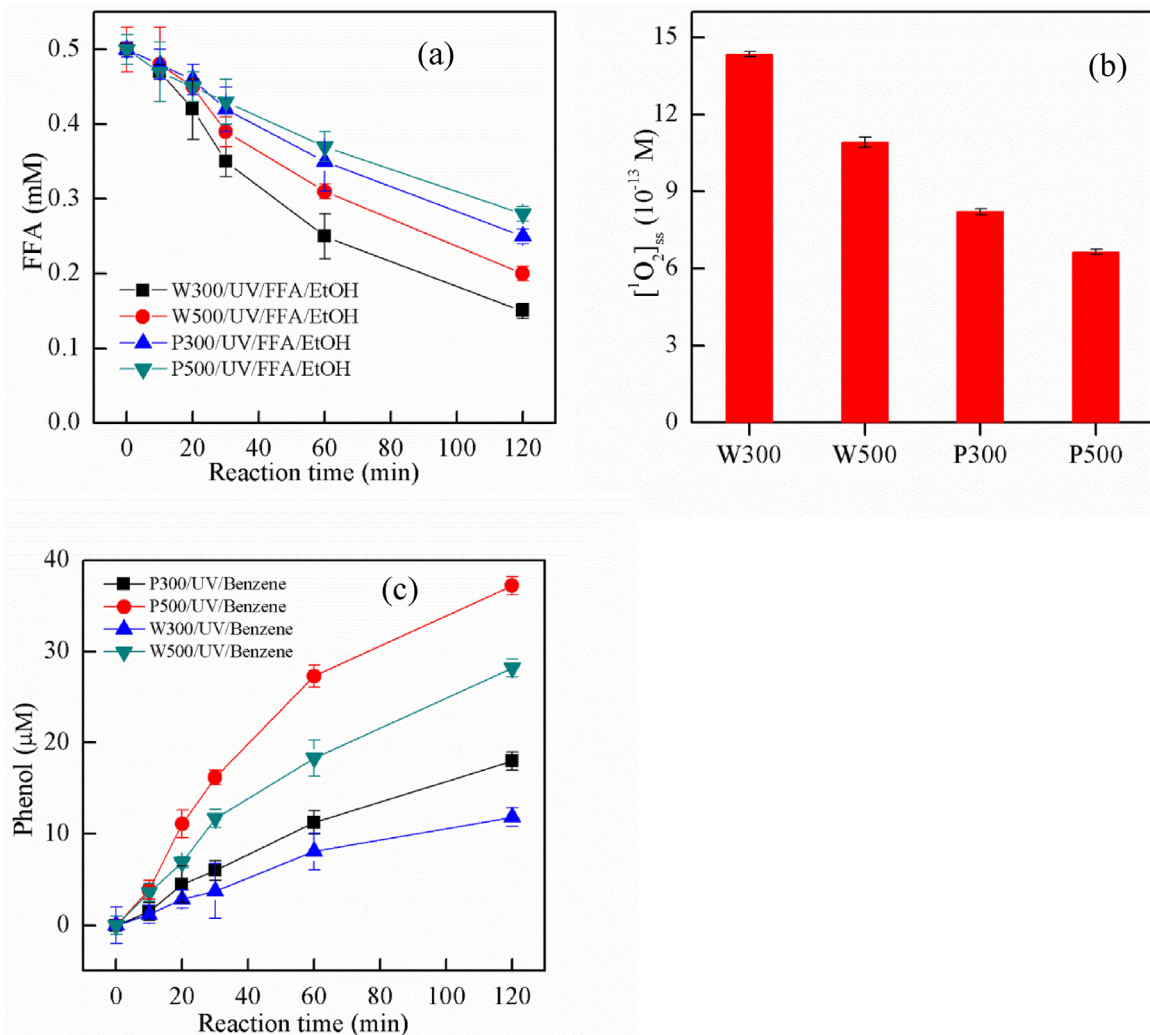


Fig. 3. Singlet oxygen and hydroxyl radical formation from biochar/UV determined with chemical probe methods: (a) FFA decay kinetics induced by $^1\text{O}_2$ oxidation, (b) steady-state concentration of $^1\text{O}_2$ calculated from the pseudo-first-order degradation kinetics of FFA, and (c) time evolution of phenol concentration formed by $\cdot\text{OH}$ and benzene. Reaction conditions: $[\text{FFA}]_0 = 0.5 \text{ mM}$, $[\text{benzene}]_0 = 2.0 \text{ mM}$, $[\text{biochar}]_0 = 0.2 \text{ g L}^{-1}$, pH 7.0 (10 mM PBS), 100-W Hg lamp, and 25 °C.

reaction (Fig. S7). Since it has been well established that DOM can induce $^1\text{O}_2$ formation under light irradiation, and the amount of $^1\text{O}_2$ formed was DOM concentration dependent [51], the formation of induced $^1\text{O}_2$ in the biochar systems might be related to the dissolution of biochar under UV irradiation.

It has been reported that $\cdot\text{OH}$ exhibits substantially high reactivity towards DEP degradation with a second order reaction rate constant of $1.96 \times 10^9 \text{ M}^{-1} \text{s}^{-1}$ [48]. The contribution of $\cdot\text{OH}$ to DEP degradation in the biochar/UV system was further determined by radical quenching studies using EtOH as a scavenger. The degradation of DEP was greatly inhibited in the presence of 200 mM EtOH in the biochar/UV systems (Fig. 2d). The degradation rate of DEP decreased from 58.9% to 17.2% for P300/UV, 72.3% to 20.2% for P500/UV, 52.3% to 23.3% for W300/UV, and 60.9% to 20.0% for W500/UV. These results indicated that $\cdot\text{OH}$ was the dominant ROS responsible for 76.7~82.8% of DEP degradation, and other ROS species would contribute to about 17.2~23.3% of DEP degradation.

3.3.2. Chemical probe methods

To further obtain quantitative information on ROS formation, EtOH/FFA and benzene were used as chemical probes to determine the concentrations of $\cdot\text{OH}$ and $^1\text{O}_2$ formed during biochar photocatalytic processes. EtOH was selected to quench the reaction between FFA and $\cdot\text{OH}$ to accurately determine $^1\text{O}_2$ concentration (Text S3)

[53]. FFA rapidly decayed in the biochar suspension under UV light within 120 min, with the concentrations decreased from 0.5 to 0.15, 0.20, 0.25 and 0.28 mM for W300, W500, P300, and P500 (0.2 g L^{-1} , pH 7.0), respectively (Fig. 3a). In contrast, the decay was insignificant ($p > 0.05$) in the biochar suspension without UV light, or under UV light in the absence of biochar particles. Furthermore, FFA disappearance curve was fitted to the pseudo-first-order equations (Fig. S8), with k_{obs} of 0.0103 min^{-1} for W300, 0.0079 min^{-1} for W500, 0.0059 min^{-1} for P300, and 0.0048 min^{-1} for P500, and the corresponding steady-state $^1\text{O}_2$ concentrations $[^1\text{O}_2]_{ss}$ were calculated to be 14.4×10^{-13} , 10.9×10^{-13} , 8.2×10^{-13} , and $6.7 \times 10^{-13} \text{ M}$, respectively (Fig. 3b). The steady-state $^1\text{O}_2$ concentrations formed in the different biochar/UV systems were in the following order: W300 > W500 > P300 > P500, which were consistent with the observed peak intensities of the EPR results.

Benzene was used as a specific probe to indirectly quantify $\cdot\text{OH}$ formation by monitoring the evolution of the reaction products of benzene with $\cdot\text{OH}$, mainly phenols, over time. As shown Fig. 3c, the total phenolic product concentrations [phenol] increased to 18.1, 37.2, 11.9, and 28.2 μM for P300/UV, P500/UV, W300/UV, and W500/UV, respectively (0.2 g L^{-1} biochar, pH 7.0, and 2.0 mM benzene). The results showed that P500 had the greatest activity to induce $\cdot\text{OH}$ formation, and the difference in photocatalytic activi-

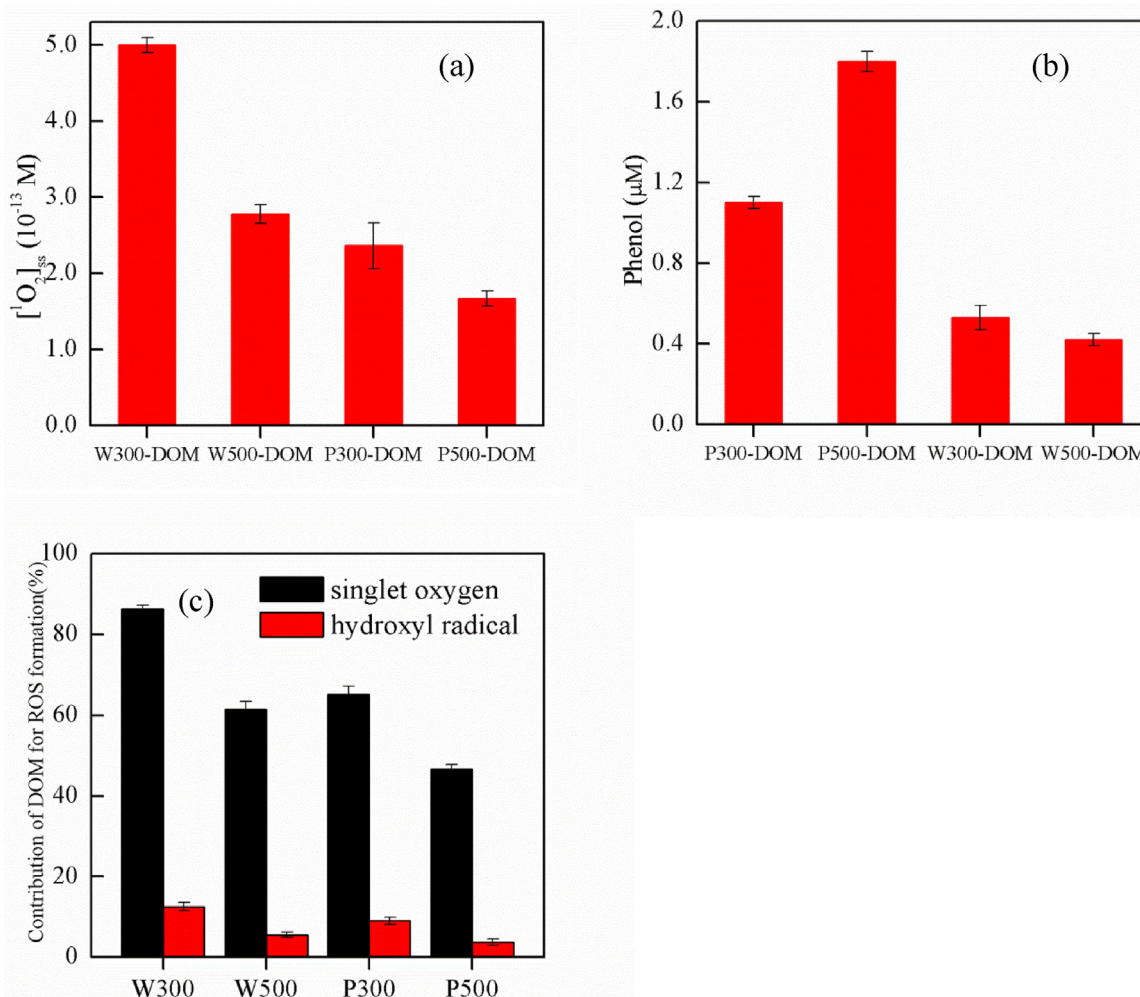


Fig. 4. Formation of $\cdot\text{OH}$ and ${}^1\text{O}_2$ from DOM extracted from biochar suspensions: (a) steady-state concentration of ${}^1\text{O}_2$ calculated from the kinetics of FFA degradation, (b) phenol concentration formed from DOM in biochar, and (c) contribution of DOM to $\cdot\text{OH}$ and ${}^1\text{O}_2$ generation in the biochar/UV system. Reaction conditions: $[\text{FFA}]_0 = 0.5 \text{ mM}$, $[\text{benzene}]_0 = 2.0 \text{ mM}$, $[\text{DOM}_{\text{P}300}] = 3.0 \text{ mg}_{\text{carbon L}^{-1}}$, $[\text{DOM}_{\text{P}500}] = 2.2 \text{ mg L}^{-1}$, $[\text{DOM}_{\text{W}300}] = 4.2 \text{ mg L}^{-1}$, $[\text{DOM}_{\text{W}500}] = 2.4 \text{ mg L}^{-1}$, pH 7.0 (10 mM PBS), 100-W Hg lamp, and 25 °C.

ties of the different biochars to induce $\cdot\text{OH}$ formation will be further discussed in the following sections.

3.4. Proposed mechanism for $\cdot\text{OH}$ and ${}^1\text{O}_2$ photogeneration from biochar suspension

3.4.1. Contribution of DOM

It has been well established that DOM can induce the formation of ROS, such as $\cdot\text{OH}$ and ${}^1\text{O}_2$, during photoreactions [34,36]. Enhanced release of DOM was observed in the biochar suspension during UV irradiation, and therefore, it was reasonable to hypothesize that biochar-derived DOM contributed substantially to $\cdot\text{OH}$ and ${}^1\text{O}_2$ formation in the biochar/UV system. The $\cdot\text{OH}$ and ${}^1\text{O}_2$ concentrations produced by biochar-derived DOM alone were quantified using benzene and FFA as probes to verify this hypothesis. The DOM contents extracted from the biochar suspensions were 4.2, 2.4, 3.0, and 2.2 $\text{mg}_{\text{carbon L}^{-1}}$ for W300, W500, P300, and P500, respectively. The EEM spectrum of DOM from biochar suspension showed strong peaks at excitation/emission wavelength pairs of 235 nm/427 nm and 280 nm/360 nm (Peaks A and B, Ex/Em), which was identified to be the fluorescence characteristics of humic acid-like compounds [48] (Fig. S9), indicating that DOM from biochar was mainly consisted of humic acid-like substances. The pseudo-first-order rate constant k_{obs} of FFA decay was 0.0036 min^{-1} for W300-DOM, 0.0020 min^{-1}

for W500-DOM, 0.0017 min^{-1} for P300-DOM, and 0.0012 min^{-1} for P500-DOM, and the corresponding $[{}^1\text{O}_2]_{ss}$ were 5.0×10^{-13} , 2.8×10^{-13} , 2.4×10^{-13} , and $1.7 \times 10^{-13} \text{ M}$, respectively (Fig. 4a, Fig. S10). Fig. 4b showed that the total concentrations of phenolic products [phenol] using benzene probe were 0.53, 0.42, 1.1, and $1.8 \mu\text{M}$ for W300, W500, P300, and P500, respectively, which indicated that biochar-derived DOM also induced a significant amount of $\cdot\text{OH}$ formation under UV light. The DOM produced $[{}^1\text{O}_2]_{ss}$ and [phenol] were normalized with respect to DOM concentration and compared with the total concentrations generated in the biochar suspension to estimate the relative contributions of biochar-derived DOM and biochar particles to ${}^1\text{O}_2$ and $\cdot\text{OH}$ formation in the system. The contributions of biochar-derived DOM to ${}^1\text{O}_2$ generation ($([{}^1\text{O}_2]_{\text{DOM}}/[{}^1\text{O}_2]_{\text{biocharsuspension}}) \times 100\%$) were calculated to be 86.3% and 65.2% for W300 and P300, respectively (Fig. 4c), indicating that biochar-derived DOM was the dominant controlling factor for ${}^1\text{O}_2$ formation for W300 and P300. To a lesser extent, biochar-derived DOM for W500 and P500 accounted for 61.5% and 46.7% of ${}^1\text{O}_2$ generation, respectively. For $\cdot\text{OH}$, all four types of biochar-derived DOM contributed to only 3.7%–12.5% of $\cdot\text{OH}$ formation based on the calculation of the concentration ratios of phenolic products ($([\text{phenol}]_{\text{DOM}}/[\text{phenol}]_{\text{biocharsuspension}}) \times 100\%$). Together, these results confirmed that biochar-derived DOM was predominantly responsible for ${}^1\text{O}_2$ formation, especially in the P300 and

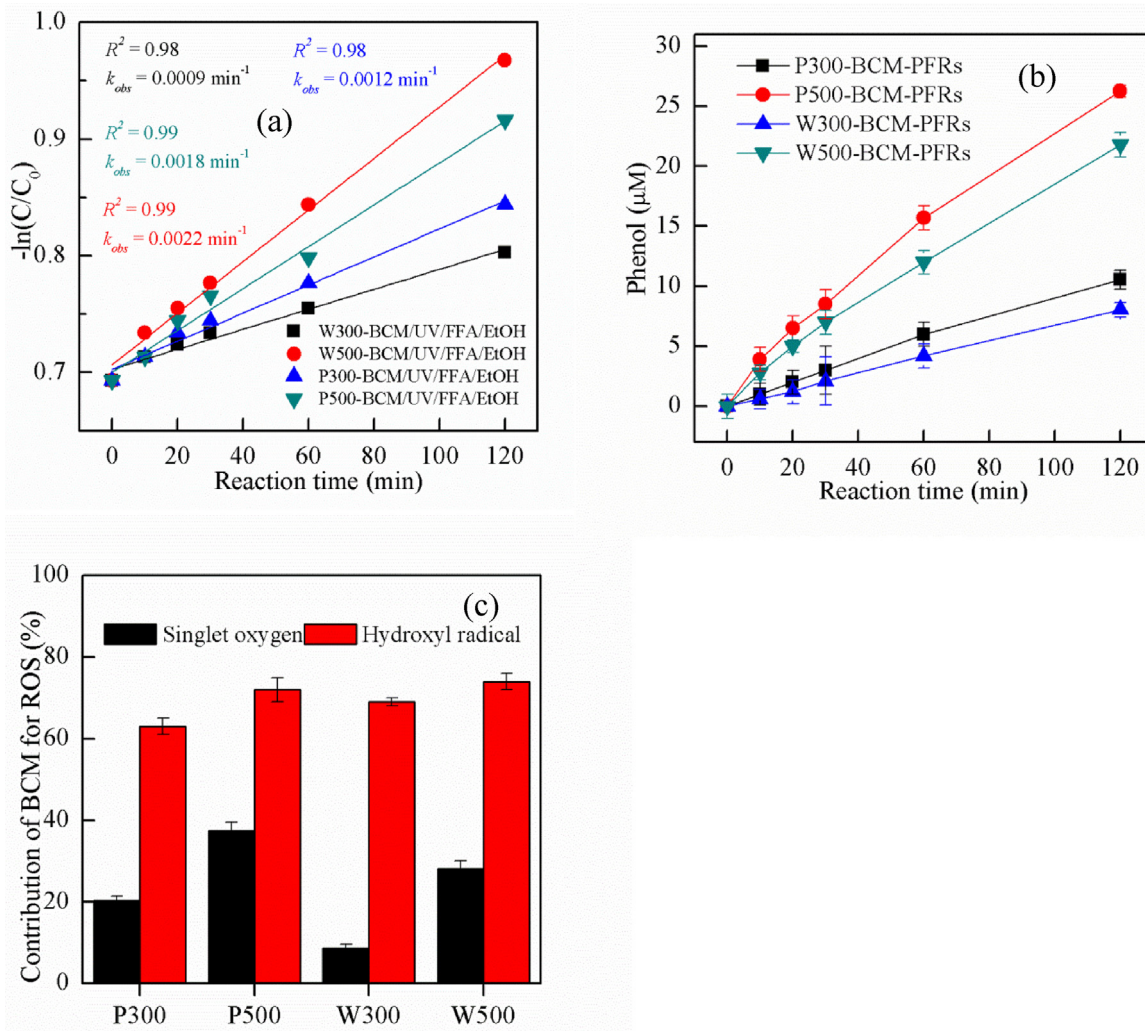


Fig. 5. Formation of $\bullet\text{OH}$ and ${}^1\text{O}_2$ from BCM suspension (biochar treated with HCl-HF to remove DOM) under UV: (a) pseudo-first-order equation fitting for FFA degradation kinetics, (b) phenol concentration formed from BCM-PFRs, and (c) contribution of BCM to $\bullet\text{OH}$ and ${}^1\text{O}_2$ generation in bulk biochar suspension under UV. Reaction conditions: $[\text{FFA}]_0 = 0.5 \text{ mM}$, $[\text{benzene}]_0 = 2.0 \text{ mM}$, $[\text{biochar}]_0 = 0.2 \text{ g L}^{-1}$, pH 7.0 (10 mM PBS), 100-W Hg lamp, and 25 °C.

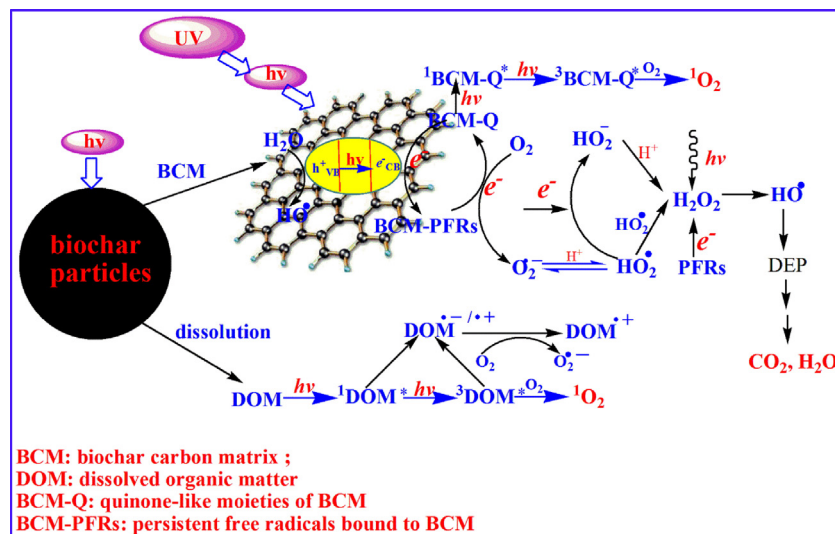
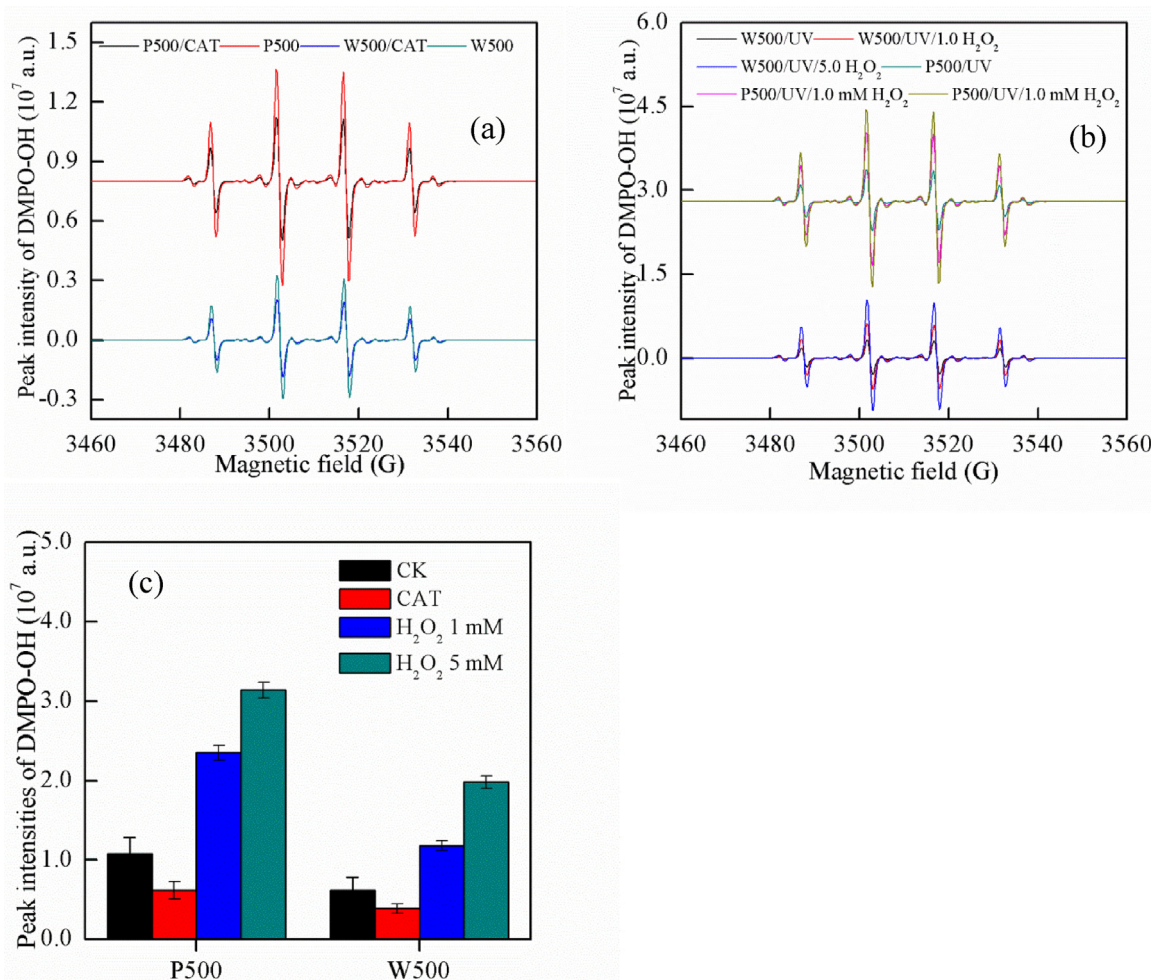
W500 suspensions, but made a limited contribution to $\bullet\text{OH}$ formation in all biochar/UV systems.

3.4.2. Contribution of biochar carbon matrix (BCM)

As discussed above, biochar-derived DOM alone did not account for all ${}^1\text{O}_2$ and $\bullet\text{OH}$ formation in the biochar/UV system. Other pathways were also responsible for ${}^1\text{O}_2$ and $\bullet\text{OH}$ formation. It has been well established that quinones or quinone-like compounds were shown to induce ${}^1\text{O}_2$ formation under light [54]. Since large quantities of quinone-like moieties were formed on the surface of biochar particles during pyrolysis [38], it was reasonable to hypothesize that the quinone-like moieties of biochar carbon matrix (BCM-Q) would also contribute to ${}^1\text{O}_2$ generation under light. In our study, the analysis of FTIR spectra showed that peaks at ~ 1613 and 1710 cm^{-1} , were attributed to the stretching vibrations of aromatic C=C, C=O and quinone C=O, which was well correlated with the previous studies [55]. Therefore, FTIR characterization together with other analysis all confirmed the existence of quinone-like structure on the surface of biochar. To confirm this, DOM-free biochar particles were prepared as surrogate of BCM by HCl-HF treatments several times until the further release of DOM fell below the detection limit ($< 0.1 \text{ mg L}^{-1}$). Therefore, the formation of ${}^1\text{O}_2$ from BCM alone under UV was determined using the FFA method (Fig. 5a). The results showed

that $[{}^1\text{O}_2]_{ss}$ was $1.25 \times 10^{-13} \text{ M}$ for W300-BCM, $3.06 \times 10^{-13} \text{ M}$ for W500-BCM, $1.67 \times 10^{-13} \text{ M}$ for P300-BCM, and $2.51 \times 10^{-13} \text{ M}$ for P500-BCM, respectively. The contribution of BCM to ${}^1\text{O}_2$ formation was assessed by normalizing $[{}^1\text{O}_2]_{ss}$ produced by BCM with respect to the total $[{}^1\text{O}_2]_{ss}$ produced in the untreated biochar suspension (Fig. 3b). The contribution of BCM, primarily BCM-Q, to ${}^1\text{O}_2$ formation was 20.4%, 37.5%, 8.68%, and 28.1% for P300, P500, W300, and W500, respectively (Fig. 5c).

PFRs are found in many carbon materials including biochars and have been reported to mediate electron transfer to O_2 and induce $\bullet\text{OH}$ formation through a metal-free Fenton-like reaction [38,42]. The concentrations of BCM bound PFRs were decreased by 15.1%, 9.8%, 21.2%, and 19.3% for W300-BCM, W500-BCM, P300-BCM, and P500-BCM, respectively, as compared to those for the untreated biochars (Fig.S5, Table S4). The ability of BCM alone to induce $\bullet\text{OH}$ formation under UV was evaluated using benzene probe method. As shown in Fig. 5b, the total phenolic product concentration [phenol] increased markedly to 10.1, 25.2, 7.8, and 20.4 μM for P300-BCM, P500-BCM, W300-BCM and W500-BCM, respectively. The contribution of PFRs to $\bullet\text{OH}$ formation was assessed by comparing [phenol] produced by BCM with that produced in the untreated biochar suspension, where [phenol] produced by BCM was normalized against PFR concentrations to compensate the PFRs loss in the biochar during HCl-HF treatment. It was calculated that the contri-

**Scheme 1.** Proposed framework for ROS formation from biochar suspension under light.**Fig. 6.** EPR spectra of biochar/UV systems in the presence of scavengers: (a) with catalase (CAT), (b) with different concentrations of added H₂O₂, and (c) changes in the peak intensities of DMPO-OH in the different reaction systems. Reaction conditions: [biochar]₀ = 0.2 g L⁻¹, [DMPO]₀ = 100 mM, [CAT]₀ = 200 units mL⁻¹, [H₂O₂]₀ = 1.0 and 5.0 mM, pH 7.0 (10 mM PBS), 100-W Hg lamp, and 25 °C.

bution of BCM-PFR to •OH formation was 63.6%, 72.5%, 69.7%, and 74.6% for P300, P500, W300 and W500, respectively. These results

indicated that BCM-PFR was the dominant factor controlling •OH generation in the biochar/UV systems.

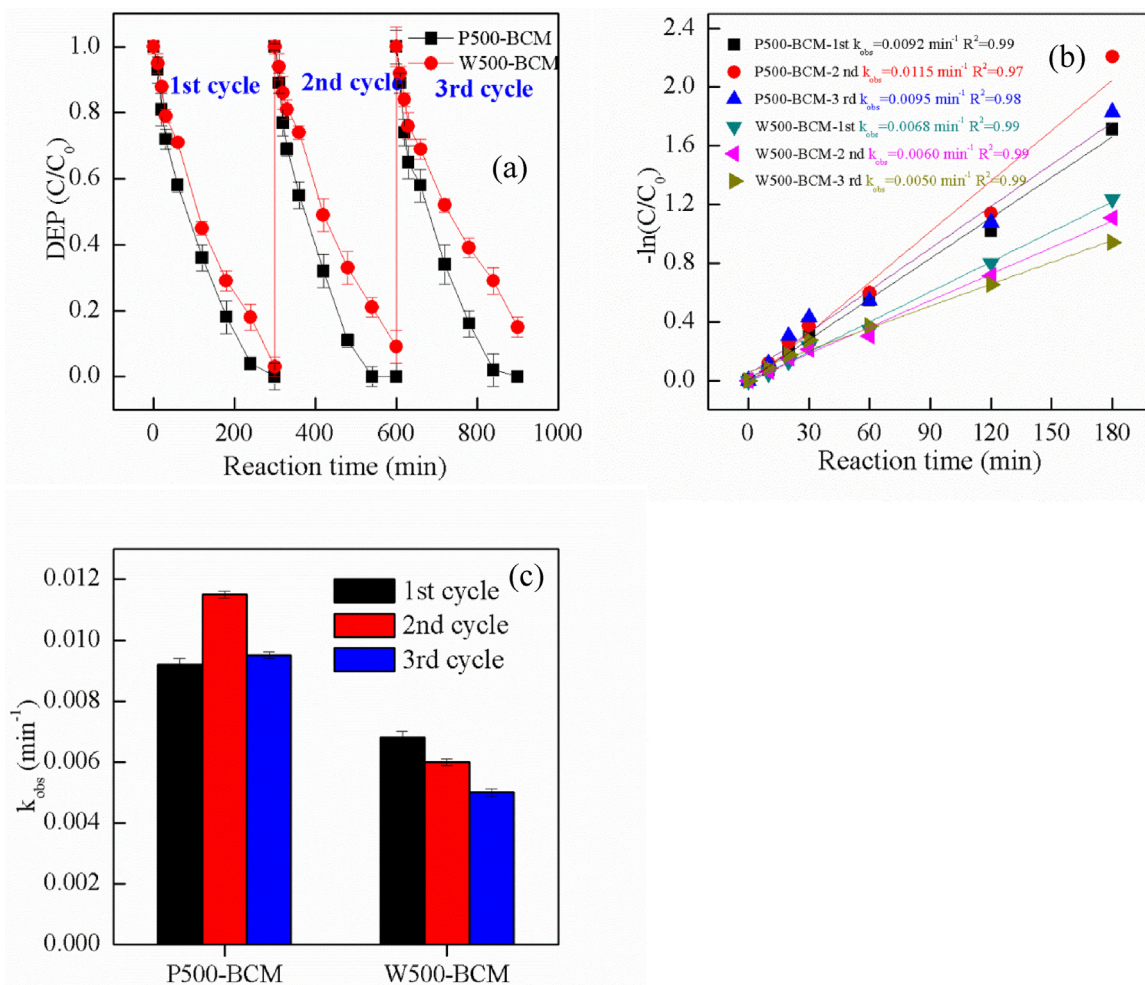


Fig. 7. Stability of biochar carbon matrix for the photodegradation of DEP under UV light with three consecutive runs: (a) kinetic of DEP degradation by BCM/UV with three runs; (b) pseudo-first-order equation for fitting the kinetics of DEP degradation; (c) changes of k_{obs} of DEP degradation among the three runs. Reaction conditions: $[DEP]_0 = 20 \text{ mg L}^{-1}$, $[P500\text{-BCM}]_0 = [W500\text{-BCM}]_0 = 0.2 \text{ g L}^{-1}$, pH 7.0 (10 mM PBS), 100-W Hg lamp, and 25 °C.

3.4.3. Proposed framework for ROS formation

Based on the discussion above, we concluded that biochar derived DOM, BCM-Q and BCM-PFRs played important roles in ROS formation in the biochar suspension under UV light, and the related mechanisms were proposed in Scheme 1. According to the mechanism of DOM-induced •OH and $^1\text{O}_2$ photogeneration reported in previous studies [33–37], similar pathways for ROS formation induced by biochar-derived DOM under UV light were formulated, in which biochar-derived DOM undergoes an energy transfer to form $^1\text{O}_2$, and an electron transfer process to yield •OH. Similarly, we proposed that the quinone-like moieties of BCM (BCM-Q) were first excited to singlet states ($^1[\text{BCM-Q}]^*$) under UV irradiation, and then $^1[\text{BCM-Q}]^*$ rapidly underwent intersystem crossing to form excited triplet states ($^3[\text{BCM-Q}]^*$) by light irradiation. $^3[\text{BCM-Q}]^*$ further reacted with dissolved oxygen via an energy transfer to yield $^1\text{O}_2$. This hypothesis was further examined by a $^3[\text{BCM-Q}]^*$ quenching study using TMP (50 μM) with FFA probe. The results showed that the disappearance of FFA in P500 and W500 suspensions was markedly suppressed in the presence of TMP, indicating strong inhibition of $^3[\text{BCM-Q}]^*$ formation and thus $^1\text{O}_2$ formation (Fig. S11). Although the accurate concentration [$^1\text{O}_2$]ss cannot be calculated because the FFA decay kinetics were too slow to be well described by a pseudo-first-order equation in the presence of TMP, it was clearly indicated that $^3[\text{BCM-Q}]^*$ was formed and primarily accounted for $^1\text{O}_2$ formation in the biochar/UV systems.

BCM-bound PFRs were assumed to mediate electron transfer to O_2 and induce •OH formation in the biochar/UV system. According to the similar mechanism of activated carbon (AC) photogeneration of ROS reported in the previous study [15,17], it was proposed that the photons from UV light would generate electron-hole pairs on the BCM via irradiation to promote electron transfer from the valence band (VB) to the conduction band (CB). Furthermore, biochar particles also contain graphite-like structure [56,57], and the electrons further transfer to the redox-active surface functional groups such as BCM-Q or C-defects to form relatively stable BCM-PFRs as evidenced by the EPR results that BCM-PFR concentrations were significantly increased under UV irradiation (Fig. S5, Table S4). For example, PFR concentrations increased from 4.57 to $14.5 (\times 10^{18} \text{ spins g}^{-1})$ for P300, and $19.6\text{--}107.9 (\times 10^{18} \text{ spins g}^{-1})$ for P500 under UV light. Moreover, Raman spectra showed that the amount of C-defects increased after the photoreactions (Fig. S4, Table S3). Since, in general, the amount of C-defects in the carbon materials was positively correlated with the PFR concentration [58], the interpretation of Raman results was consistent with the EPR evidence and indicated that more BCM-PFRs were produced on biochar under light.

BCM-bound PFRs react with dissolved oxygen to yield $\text{O}_2^{\bullet-}$, which can further accept electrons or disproportionate to form H_2O_2 . Then H_2O_2 mediates •OH formation via two possible pathways, a BCM-PFR activation process and a photo-Fenton reaction with UV light. The contribution of such H_2O_2 -dependent pathways

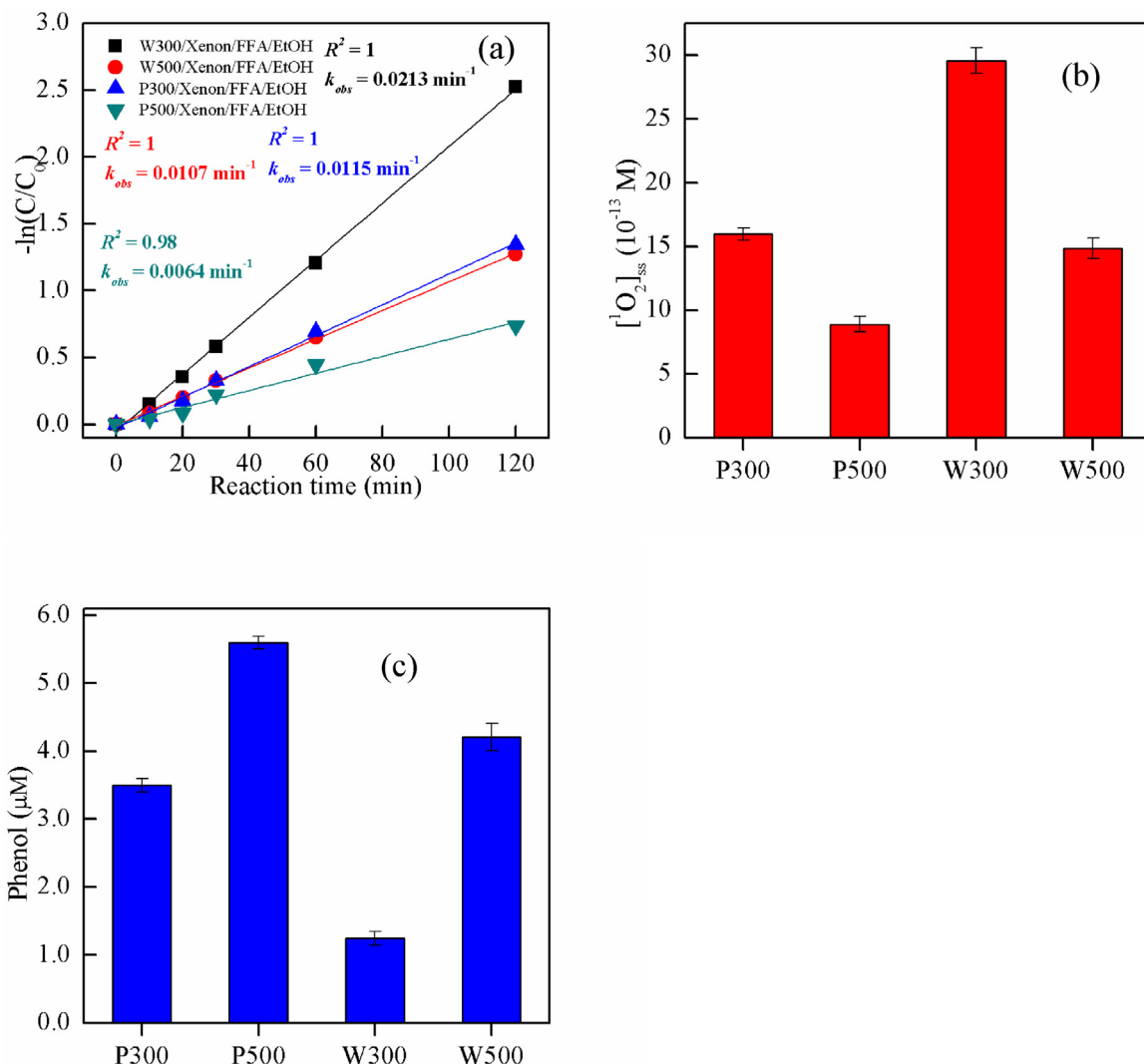


Fig. 8. Determination of $\cdot\text{OH}$ and ${}^1\text{O}_2$ formed from biochar suspension under solar light: (a) kinetics of FFA decay in biochar suspension under xenon light, (b) steady-state concentration of ${}^1\text{O}_2$ calculated from the k_{obs} of FFA degradation, and (c) concentration of phenol formed by benzene and $\cdot\text{OH}$ in biochar/xenon. Reaction conditions: $[\text{FFA}]_0 = 0.5 \text{ mM}$, $[\text{benzene}]_0 = 2.0 \text{ mM}$, $[\text{biochar}]_0 = 0.2 \text{ g/L}$, pH 7.0 (10 mM PBS), 500-W Xe lamp, and 25 °C.

to $\cdot\text{OH}$ formation was evaluated by EPR coupled with additions of H_2O_2 or catalase (CAT), a H_2O_2 quencher that can decompose H_2O_2 to H_2O and O_2 . The DMPO–OH peak intensities in the presence of CAT decreased markedly in the biochar/UV systems (Fig. 6). In contrast, the DMPO–OH peak intensities increased 2.2-fold with the addition of 1.0 mM H_2O_2 into the reaction system, and about 3.1-fold when the H_2O_2 concentration was increased to 5.0 mM. These results suggested that increasing the H_2O_2 concentration favored $\cdot\text{OH}$ production in the reaction system, and further supported that the H_2O_2 -dependent pathways play an important role in OH formation in the biochar/UV system.

3.4.4. Other potential $\cdot\text{OH}$ sources

According to the results shown in Figs. 4 and 5 and the related discussion, the contribution of biochar-derived DOM to $\cdot\text{OH}$ formation was 3.7%–12.5%, and biochar bound PFRs contributed 63.6%–74.6%, indicating that some unidentified processes would account for 17.8%–26.7% of $\cdot\text{OH}$ generation in the biochar/UV system. Other likely pathways for $\cdot\text{OH}$ formation have been suggested including H-atom abstraction from water by some DOM excited states (${}^3\text{DOM}^*$, ${}^1\text{DOM}^*$) or charge transfer species ($\text{DOM}^{\bullet-}/{}^{\bullet+}$) or similarly the excited states of BCM-Q [34,59], but the mechanism has not yet been fully established. Furthermore, the photogener-

ated electron/hole pairs on BCM surface can be effectively separated and stabilized via surface charge transfers, and the oxidative holes could also contribute to the formation of $\cdot\text{OH}$ from the oxidation of water.

3.4.5. Reusability of biochar carbon matrix for the photocatalytic degradation of DEP

To evaluate the reusability of biochar in the formation of ROS for contaminant degradation under UV, DEP degradation by P500-BCM and W500-BCM was investigated in three consecutive runs. BCM particles were collected after HCl/HF treatments, and filtrated and freeze-dried after the photochemical reactions. All the experiments were performed with 0.2 g/L BCM particles, 20 mg/L DEP, and at pH 7.0 (PBS) under UV light. As illustrated in Fig. 7a, DEP was almost completely degraded within 300 min by both P500-BCM/UV and W500-BCM/UV. In the following two consecutive runs, DEP were also effectively degraded by BCM/UV, but slight different kinetic rates of DEP degradation were observed in P500-BCM and W500-BCM. For W500-BCM, the ability of inducing DEP degradation slightly decreased, and k_{obs} of DEP degradation decreased from 0.0068 min^{-1} to 0.0050 min^{-1} in the three successive runs (Fig. 7b). However, for P500-BCM, k_{obs} of DEP degradation increased from 0.0092 min^{-1} to 0.0115 min^{-1} for the 2nd run and then decreased

to 0.0095 min^{-1} for the 3rd run. P500-BCM was slightly more stable than W500-BCM for the catalytic degradation of DEP under irradiation. The good photostability of both biochars was probably due to the accumulation of BCM-PFR and the slow decomposition of BCM under UV irradiation.

3.5. Formation of ROS from biochar suspension under solar light

To further assess the ability of biochar to induce ROS formation under the simulated solar light, ROS formation in a biochar suspension was studied under a xenon lamp (500 W). As shown in Fig. 8a, FFA decay kinetics studies in the biochar suspension under simulated solar light, suggested the steady-state $^1\text{O}_2$ concentrations [$^1\text{O}_2]_{ss}$ reached $16.0 \times 10^{-13} \text{ M}$ for P300, $8.9 \times 10^{-13} \text{ M}$ for P500, $29.6 \times 10^{-13} \text{ M}$ for W300, and $14.9 \times 10^{-13} \text{ M}$ for W500, respectively (Fig. 8b). The total phenolic product concentrations [phenol] formed using benzene probe were 3.5, 5.6, 1.3, and $4.2 \mu\text{M}$ for P300, P500, W300, and W500, respectively (Fig. 8c). These results indicated that biochar particles also induced ROS formation under solar light following the similar pathways under UV light as discussed above.

4. Conclusions

The photochemical properties of biochar are relatively unknown; however, it is crucial part for evaluating the effects of biochar on the transport and transformation of organic contaminants in aquatic systems. The present study was the first study that systematically explored the photochemical reactivities of biochar particles. The ROS formation pathways in the biochar suspension under light and the reaction mechanisms were thoroughly investigated. It is verified that biochar particles is capable of inducing DEP degradation under both UV and solar lights, by formation of ROS species such as $\cdot\text{OH}$ and $^1\text{O}_2$, as identified by EPR technique and free radical quenching studies. In addition to DOM derived from biochar particles, biochar carbon matrix (BCM) can also induce the formation of $\cdot\text{OH}$ and $^1\text{O}_2$ in the presence of UV light. The contributions of biochar-derived DOM and BCM to $\cdot\text{OH}$ and $^1\text{O}_2$ were quantitatively evaluated and it was found that biochar-derived DOM generated 46.7%–86.3% of $^1\text{O}_2$ and 3.7%–12.5% of $\cdot\text{OH}$, while BCM accounted for 63.6%–74.6% of $\cdot\text{OH}$ and 10%–44.7% of $^1\text{O}_2$ formation. These results indicate that biochar containing a large amount of DOM exhibits a relatively higher ability to induce the formation of $^1\text{O}_2$, while biochar containing a high amount of surface bound-PFRs can effectively induce the formation of more $\cdot\text{OH}$ under light. Furthermore, BCM exhibited excellent reusability towards the photocatalytic degradation of DEP.

The finding of this study indicates that biochar particles not only can adsorb contaminants, but also play an important role in the phototransformation of contaminants in the natural environment. From an engineering standpoint, this study establishes a novel photochemical process based on biochar that could be applied to the degradation of organic contaminants in wastewater. It can be used in combination with the traditional photocatalysts, which help further enhance the photocatalytic activity and feasibility for contaminant degradation in water.

Acknowledgments

This work was supported by grants from the National Key Research and Development Program of China (2016YFD0800204), the National Natural Science Foundation of China (21537002, 41671478), the Natural Science Foundation of Jiangsu Province of China (BK20141047), and Youth Innovation Promotion Association

of CAS (2014270). We thank Dr. Qinglong Fu for the analysis of EEM data.

Appendix A. Supplementary data

Supplementary data associated with this article can be found, in the online version, at <http://dx.doi.org/10.1016/j.apcatb.2017.05.036>.

References

- [1] S.N. Frank, A.J. Bard, J. Am. Chem. Soc. 99 (1977) 303–304.
- [2] M. Pelaez, N.T. Nolan, S.C. Pillai, M.K. Serry, P. Falaras, A.G. Kontos, P.S.M. Dunlop, J.W.J. Hamilton, J.A. Byrne, K.O. Shea, M.H. Entezari, D.D. Dionysiou, Appl. Catal. B: Environ. 125 (2012) 331–349.
- [3] C. Bojer, J. Schöbel, T. Martin, M. Ertl, H. Schmalz, J. Breu, Appl. Catal. B: Environ. 204 (2017) 561–565.
- [4] X. Bai, C. Sun, D. Liu, X. Luo, D. Li, J. Wang, N. Wang, X. Chang, R. Zong, Y. Zhu, Appl. Catal. B: Environ. 204 (2017) 11–20.
- [5] F. Sannino, D. Pirozzini, G. Vitiello, G. D'errico, A. Aronne, E. Fanelli, P. Pernice, Appl. Catal. B: Environ. 156–157 (2014) 101–107.
- [6] M. Aslam, M.T. Qamar, M.T. Soomro, I.M.I. Ismail, N. Salah, T.I. Almeelbi, M.A. Gondal, A. Hameed, Appl. Catal. B: Environ. 180 (2016) 391–402.
- [7] A. Hernandez-Gordillo, A.G. Romero, F. Tzompantzi, R. Gómez, Appl. Catal. B: Environ. 144 (2014) 507–513.
- [8] J. Matos, J. Laine, J.M. Herrmann, J. Catal. 200 (2001) 10–20.
- [9] R. Leary, A. Westwood, Carbon 49 (2011) 741–772.
- [10] G.L. Puma, O. Bono, D. Krishniah, J.G. Collin, J. Hazard. Mater. 157 (2008) 209–219.
- [11] J. Matos, J. Laine, J.M. Herrmann, Synergy effect in the photocatalytic degradation of phenol on the suspended mixture of titania and activated carbon, Appl. Catal. B: Environ. 18 (1998) 281–291.
- [12] J. Matos, J. Laine, J.H. Hermann, D. Uzcategui, J.L. Brito, Influence of activated carbon upon titania on aqueous photocatalytic consecutive runs of phenol photodegradation, Appl. Catal. B: Environ. 70 (2007) 461–469.
- [13] J.L. Faria, W. Wang, Carbon materials in photocatalysis, in: P. Serp, J.L. Figueiredo (Eds.), Carbon Materials for Catalysis, John Wiley & Sons, Hoboken, NJ, 2009, pp. 481–506.
- [14] L.F. Velasco, I.M. Fonseca, J.B. Parra, J.C. Lima, C.O. Ania, Carbon 50 (2012) 249–258.
- [15] I. Velo-Gala, J.J. López-Peña, M. Sánchez-Polo, J. Rivera-Utrilla, Appl. Catal. B: Environ. 142–143 (2013) 694–704.
- [16] L.F. Velasco, R.J. Carmona, J. Matos, C.O. Ania, Carbon 73 (2014) 206–215.
- [17] I. Velo-Gala, J.J. López-Peña, M. Sánchez-Polo, J. Rivera-Utrilla, Appl. Catal. B: Environ. 207 (2017) 412–423.
- [18] M.S. Mauter, M. Elimelech, Environ. Sci. Technol. 42 (2008) 5843–5859.
- [19] C.Y. Chen, C.T. Jafvert, Environ. Sci. Technol. 44 (2010) 6674–6679.
- [20] W.C. Hou, I. Chowdhury, D. Goodwin, M. Henderson, D.H. Fairbrother, D. Bouchard, R.G. Zepp, Environ. Sci. Technol. 49 (2015) 3435–3443.
- [21] J. Lee, Y.D. Yamakoshi, J.B. Hughes, J. Kim, Environ. Sci. Technol. 42 (2008) 3459–3464.
- [22] J.P. Kamat, T.P.A. Devasagayam, K.I. Priyadarsini, H. Mohan, Toxicology 155 (2000) 55–61.
- [23] H. Tokuyama, S. Yamago, E. Nakamura, T. Shiraki, Y. Sugiura, J. Am. Chem. Soc. 115 (1993) 7918–7919.
- [24] J. Lehmann, J. Gaunt, M. Rondon, Mitig. Adapt. Strategies Glob. Change 11 (2006) 403–427.
- [25] R. Cernansky, Nature 517 (2015) 258–260.
- [26] J.J. Manyà, Environ. Sci. Technol. 46 (2012) 7939–7954.
- [27] B. Chen, D. Zhou, L. Zhu, Environ. Sci. Technol. 42 (2008) 5137–5143.
- [28] X.D. Cao, L. Ma, B. Gao, W. Harris, Environ. Sci. Technol. 43 (2009) 3285–3291.
- [29] D.J. Wang, W. Zhang, X.Z. Hao, D.M. Zhou, Environ. Sci. Technol. 47 (2013) 821–828.
- [30] W.H. Clements, R.G. Stahl Jr., R.C. Landis, Environ. Sci. Technol. 49 (2015) 14649–14654.
- [31] X. Qu, H. Fu, J. Mao, Y. Ran, D. Zhang, D. Zhu, Carbon 96 (2016) 759–767.
- [32] R. Jaffe, Y. Ding, J. Niggemann, A.V. Vahatalo, A. Stubbins, R.G.M. Spencer, J. Campbell, T. Dittmar, Science 340 (2013) 345–347.
- [33] S. Garg, A.L. Rose, T.D. Waite, Geochim. Cosmochim. Acta 75 (2011) 4310–4320.
- [34] R.G. Zepp, P.F. Schlotzhauer, R.M. Sink, Environ. Sci. Technol. 19 (1985) 74–81.
- [35] D.E. Latch, K. McNeill, Science 311 (2006) 1743–1747.
- [36] A.L. Boreen, B.L. Edlund, J.B. Cotner, K. McNeill, Environ. Sci. Technol. 42 (2008) 5492–5498.
- [37] K. Mopper, X. Zhou, Science 250 (1990) 661–663.
- [38] G.D. Fang, J. Gao, C. Liu, D.D. Dionysiou, Y. Wang, D.M. Zhou, Environ. Sci. Technol. 48 (2014) 1902–1910.
- [39] S. Liao, B. Pan, H. Li, D. Zhang, B. Xing, Environ. Sci. Technol. 48 (2014) 8581–8587.
- [40] G.D. Fang, J. Gao, C. Liu, D.D. Dionysiou, D.M. Zhou, Environ. Sci. Technol. 49 (2015) 5645–5653.
- [41] G. Fang, C. Zhu, D.D. Dionysiou, J. Gao, D. Zhou, Bioresour. Technol. 176 (2015) 210–217.

- [42] J. Yang, B. Pan, H. Li, S. Liao, D. Zhang, M. Wu, B. Xing, *Environ. Sci. Technol.* 50 (2016) 694–700.
- [43] Z.F. Huang, H.W. Bao, Y.Y. Yao, W.Y. Lu, W.X. Chen, *Appl. Catal. B: Environ.* 154–155 (2014) 36–43.
- [44] L. Luo, D. Wu, D. Dai, Z. Yang, L. Chen, Q. Liu, J. He, Y. Yao, *Appl. Catal. B: Environ.* 205 (2017) 404–411.
- [45] L. Klüpfel, M. Keiluweit, M. Kleber, M. Sander, *Environ. Sci. Technol.* 48 (2014) 5601–5611.
- [46] J.M. Saquing, Y. Yu, P.C. Chiu, *Environ. Sci. Technol. Lett.* 3 (2016) 62–66.
- [47] S. Xu, D. Adhikari, R. Huang, H. Zhang, Y. Tang, E. Roden, Y. Yang, *Environ. Sci. Technol.* 50 (2016) 2389–2395.
- [48] H. Fu, H. Liu, J. Mao, W. Chu, Q. Li, P.J.J. Alvarez, X. Qu, D. Zhu, *Environ. Sci. Technol.* 50 (2016) 1218–1226.
- [49] B. Xu, N. Gao, X. Sun, S. Xia, M. Rui, M. Simonnot, C. Causserand, J. Zhao, *J. Hazard. Mater. B* 139 (2007) 132–139.
- [50] X.D. Zhu, D.M. Zhou, Y.J. Wang, L. Cang, G.D. Fang, J.X. Fan, *J. Soils Sediments* 12 (2012) 1371–1379.
- [51] R.L. Frost, J. Cejka, M.L. Weier, W. Martens, *J. Raman Spectrosc.* 37 (2006) 538–551.
- [52] S. Pou, D.J. Hassett, B.E. Britigan, M.S. Cohen, G.M. Rosen, *Anal. Biochem.* 177 (1989) 1–6.
- [53] S. Mostafa, F.L. Rosario-Ortiz, *Environ. Sci. Technol.* 47 (2013) 8179–8186.
- [54] R. Marquardt, S. Grandjean, R. Bonneau, *Photobiolo. A Chem.* 69 (1992) 143–153.
- [55] F.N.D. Mukome, A.L.D. Kilcoyne, S.J. Parikh, *Soil Sci. Soc. Am. J.* 78 (2014) 1632–1640.
- [56] M. Keiluweit, P. Nico, M. Johnson, M. Kleber, *Environ. Sci. Technol.* 44 (2010) 1247–1253.
- [57] A. Downie, A. Crosky, P. Munroe, Physical properties of biochar, in: J. Lehmann, S. Joseph (Eds.), *Biochar for Environmental Management: Science and Technology*, Earthscan, London, 2009, pp. 13–32.
- [58] G.D. Fang, C. Liu, J. Gao, D.M. Zhou, *Ind. Eng. Chem. Res.* 53 (2014) 19925–19933.
- [59] J. Wenk, S.N. Eustis, K. McNeill, S. Canonica, *Environ. Sci. Technol.* 47 (2013) 12802–12810.